Reduced upper ocean turbulence and changes to bubble size distributions during large downward heat flux events

Svein Vagle,[1] Johannes Gemmrich,[2] and Helen Czerski[3]

Received 18 May 2011; revised 9 December 2011; accepted 11 December 2011; published 9 February 2012.

[1] During the Radiance in a Dynamic Ocean (RaDyO) field study south of Hawaii in September 2009, simultaneous observations of total heat flux, upper ocean turbulence, and bubble size distributions suggest that large downward heat flux modulates the upper ocean turbulence dissipation rates and subsequently the upper ocean bubble field. The observations show that the turbulence dissipation rates near the ocean surface are reduced by a factor of 10 during periods with high downward heat flux (>400 W m^{-2}). Simultaneously, the observations of bubble size distributions at a depth of 0.5 m show that there were significantly lower concentrations of bubbles with radii >100 μm than during a winter study in the Gulf of Mexico. Also, the number of bubbles with radii >200 μm is found to be dependent on the heat flux, with fewer such bubbles during stable (positive heat flux) conditions. The reduced number of larger bubbles reduces the effect of the bubble field on optical reflectance by up to a factor of 3 compared to other locations at similar wind speeds.

Citation: Vagle, S., J. Gemmrich, and H. Czerski (2012), Reduced upper ocean turbulence and changes to bubble size distributions during large downward heat flux events, *J. Geophys. Res.*, *117*, C00H16, doi:10.1029/2011JC007308.

1. Introduction

[2] Bubbles are a ubiquitous feature of the upper ocean boundary layer. Even at very low wind speeds they are generally present, especially in supersaturated conditions, and at higher wind speeds they occur in dense clouds extending many meters in depth. The exact role these bubbles may play in affecting near-surface layer light scattering is still not well understood, but there is growing evidence that it may be significant [*Stramski*, 1994; *Zhang et al.*, 1998; *Terrill et al.*, 1998; *Stramski and Tegowski*, 2001].

[3] Most of the upper ocean boundary layer bubbles are a result of breaking wind generated waves that appear when the wind speed exceeds approximately 3 m s^{-1} [*Thorpe*, 1992]. Photographic techniques have been used to study the mechanisms involved in the initial jets of water plunging forward from the breaking crests, entraining long slender air cavities which quickly become unstable and break up into streams of bubbles [*Deane and Stokes*, 2002]. These high air fraction plumes quickly evolve into more diffuse plumes by advection due to surface currents, turbulence, buoyancy, and gas exchange. The resulting air fractions are orders of magnitude less than the initial air fraction and can reach values up to 10^{-5}. The subsequent bubble field is often observed as bubble plumes extending tens of meters into the mixed layer, mainly due to Langmuir circulation [e.g., *Vagle et al.*, 2010].

[4] Turbulence plays a major part in the dynamics of the upper ocean boundary layer. Near the surface the turbulence field is commonly dominated by turbulence generated in steep and breaking waves [*Gemmrich and Farmer*, 2004; *Gemmrich*, 2010]. Wave induced turbulence is responsible for the breakup of bubbles [*Garrett et al.*, 2000; *Gemmrich*, 2010] and is an important mechanism for transporting bubbles from the active breakers and into the water column. Also, because bubbles of different sizes have different rise speeds, turbulent eddies will be important as a sorting process in terms of the local bubble size distribution and therefore the local air fraction.

[5] The present investigation was part of the Hawaii Radiance in a Dynamic Ocean (RaDyO) study (the ongoing special section "Recent Advances in the Study of Optical Variability in the Near-Surface and Upper Ocean" in *Journal of Geophysical Research*), which presented us with an opportunity to investigate the role of strong downward heat flux on near-surface turbulence and subsequently on the bubble field in the upper ocean boundary layer. The results are being used to infer possible effects on the near-surface optical radiance field.

2. Measurement Approach

[6] The measurements required for studying the effect of near-surface stratification on turbulence and bubble size distributions were obtained from instruments mounted on the hull of R/P *FLIP*, on a small wave-following float deployed from *FLIP* (Figure 1), and on a small surface-

[1]Institute of Ocean Sciences, Fisheries and Oceans Canada, Sidney, British Columbia, Canada.
[2]Department of Physics and Astronomy, University of Victoria, Victoria, British Columbia, Canada.
[3]Institute of Sound and Vibration Research, University of Southampton, Southampton, UK.

0148-0227/12/2011JC007308

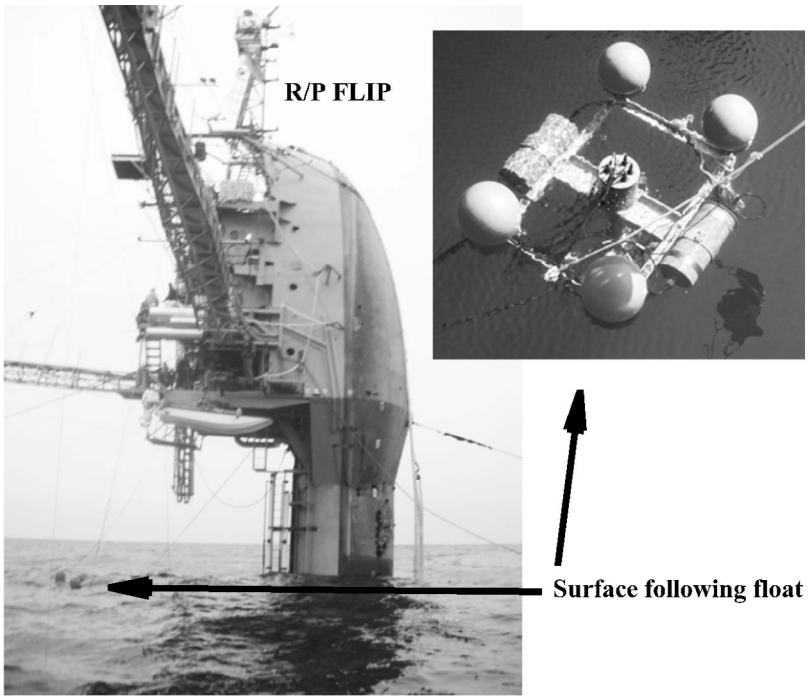

Figure 1. Images showing the surface-following float equipped with an acoustical resonator, three 2 MHz Dopbeam coherent Doppler sonars and a thermistor at 0.4 m, tethered to R/P *FLIP*. In addition, thermistors and 100 kHz backscatter side scan transducers were mounted on *FLIP*'s hull. A second small float (not shown) with a thermistor at 0.1 m was deployed from R/V *Kilo Moana* approximately 2 km away for shorter periods.

following float tethered to R/V *Kilo Moana* approximately 2 km away from *FLIP*. Four narrow-beam 100 kHz Doppler sonars were directed at four orthogonal directions horizontally away from *FLIP* at a mean depth of 34 m. These sonars have azimuthal beam angles of 1.5° and 60° beam widths in elevation. All four transducers were tilted up from the horizontal by 30° to allow the edge of the beam to reach the ocean surface straight above. The pulse repetition rate of the sonars was set to 1 Hz during the period considered here. The backscatter data from these sonars were used to estimate the total vertical extent of the local bubble field as well as a measure of the spatial extent and variability in the bubble field covering the area from *FLIP* and out to a range of 300 m. This sonar system was not calibrated and could therefore not be used to obtain absolute measurements of the bubble concentration.

[7] The upper ocean temperature gradient was obtained with a vertical array of RBR TR-1050 internally recording thermistors deployed at depths of 3, 7, and 15 m on the hull of *FLIP*. The sensors were programmed to record the temperature field every 20 s throughout the study. Due to the low number of thermistors and the resulting sparse vertical resolution (first sensor at 3 m), this array could not be used to determine the temperature gradient right up near the surface. For additional information about the near-surface temperature gradients we periodically deployed a small surface-following float from *FLIP*, with a thermistor at a nominal depth of 0.4 m (Figure 1). And for approximately 2 h d^{-1}, a small float with a thermistor at 0.1 m was deployed from R/V *Kilo Moana*, approximately 2 km away.

[8] The in situ bubble size distribution was measured every 2–3 s using the acoustical resonator technique [*Farmer et al.*, 1998, 2005; *Czerski et al.*, 2011a], where a freely flooding resonator was deployed at a nominal depth of 0.5 m on the small surface-following float between two near orthogonal booms on R/P *FLIP* (Figure 1). The acoustical resonator is one of several instruments that allow for measurements of bubble size distributions through inversion of the bulk acoustic properties of the fluid. *Farmer et al.* [1998] provide detailed mathematical analysis of the resonator operation and the inversion approach, developed by *Commander and McDonald* [1991], used to obtain bubble size distributions from attenuation measurements. A recent investigation by *Czerski et al.* [2011a] has developed a simpler and more direct approach to calculating frequency-dependent attenuation from resonator data. However, this approach requires sensors with a better signal-to-noise ratio than was available during the present study. We will therefore use the approach developed by *Farmer et al.* [1998] in the subsequent analysis, taking into consideration the reverberation effects discussed by *Farmer et al.* [2005].

[9] The near-surface turbulence field was monitored with a set of three 2 MHz single beam Doppler sonars (Dopbeam, Sontek) mounted on the surface-following *FLIP* float. The Dopbeams acquired radial velocities in 120 6 $\times$ 10^{-3} m range bins along a path starting 0.14 m ahead of each sensor, and at a rate of 20 Hz. (These are the same settings as used by *Gemmrich* [2010].) Thus, the maximum range of the velocity profiles is 0.72 m, whereas the backscatter was recorded over 450 bins, i.e., a profile range of up to 2.5 m. The shallowest sensor was vertically upward pointing with

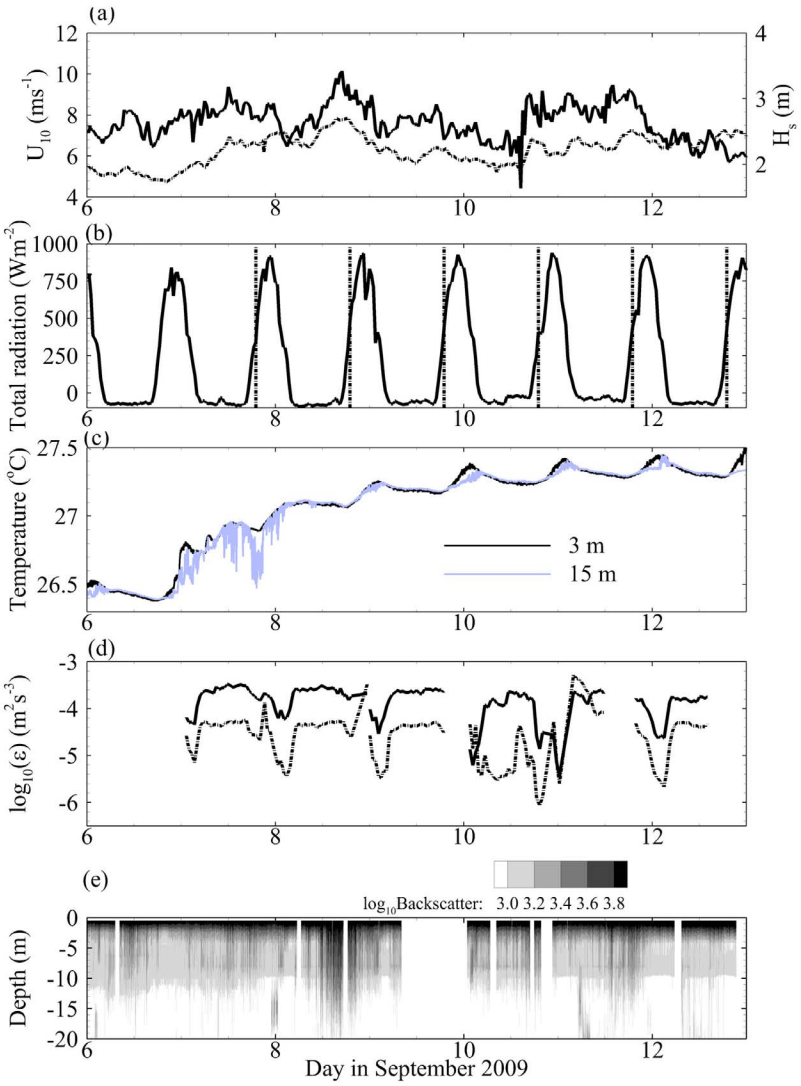

Figure 2. (a) Seven day records of wind speed at 10 m, U_{10}, significant wave height, H_s. (b) Measured total heat flux. The vertical dashed lines show the periods when the small thermistor float was deployed from the *Kilo Moana*. (c) Temperatures at 3 and 15 m below the surface collected from R/P *FLIP* during the experiment. (d) The turbulence dissipation rate, ε, averaged between depths of 0.14 and 0.75 m (dash-dotted line) and between 1.04 and 1.76 m (solid line). (e) Noncalibrated 100 kHz backscatter intensities from transducer mounted at a depth of 34 m on *FLIP*'s hull.

the measurements starting at 0.72 m below the mean water level. The second sonar was downward oriented, profiling the velocity at distances from 1.04 to 1.76 m below the mean water line and measuring acoustical backscatter between depths of 1.04–3.54 m. The deepest sensor was mounted horizontally at a mean depth of 1.3 m and was only used to monitor bubble plumes from the backscattered signal. The float was tracking the vertical displacement of larger waves, but was not able to follow accurately shorter superimposed waves. However, the instantaneous surface is resolved by the upward-looking backscatter profile [*Gemmrich*, 2010], and in the following analysis the velocity and backscatter measurements are referenced to the instantaneous free surface. The spectrum of the surface elevation not resolved by the float motion peaks at 0.5 Hz and has a standard deviation of 0.06 m, with only small variations throughout the experiment.

[10] Following *Gemmrich* [2010] the turbulence kinetic energy (TKE) dissipation rate $\varepsilon(z, t)$ is estimated based on centered second-order structure functions

$$D(z,s,\overline{t}) = \left\langle (v'(z-s/2,t) - v'(z+s/2,t))^2 \right\rangle \qquad (1)$$

and

$$\varepsilon(z,t) = C^{-3/2} s^{-1} D(z,s,t)^{3/2}, \qquad (2)$$

where z is the depth from the free surface, s the range at which the structure function is evaluated and the constant $C = 2.0$. Estimating dissipation from structure functions

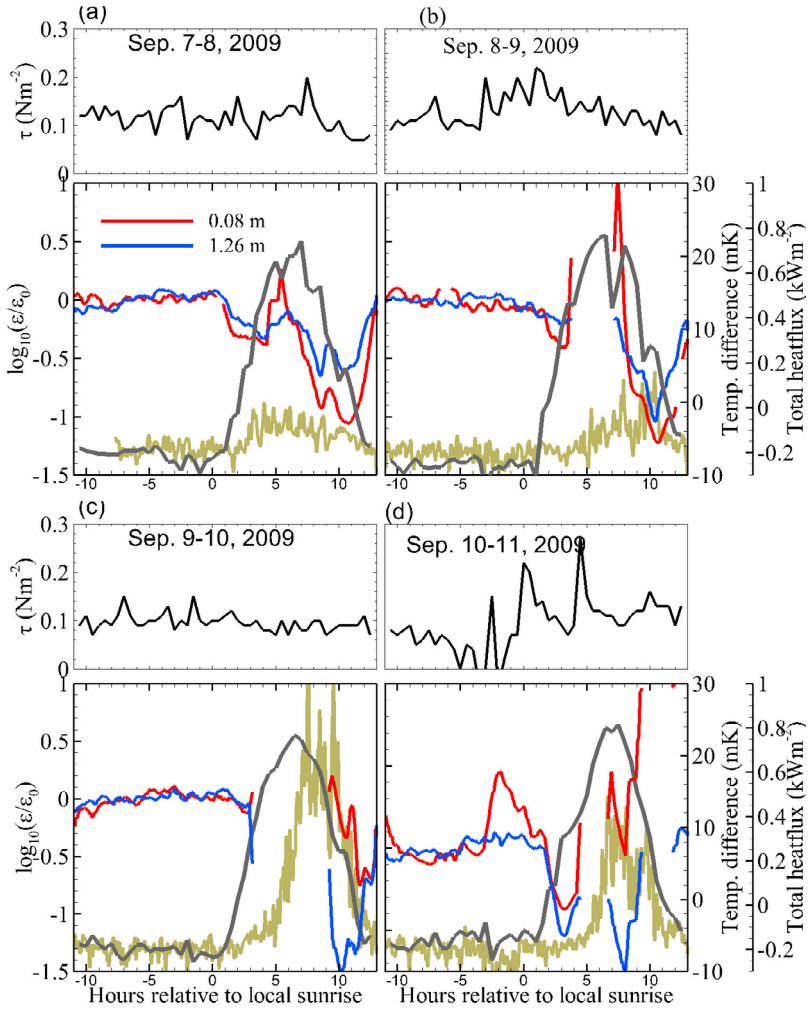

Figure 3. Wind stress, τ, the ratio of turbulent dissipation rate ε normalized by the averaged dissipation rates from -10 to -2 h, ε_0, for two depths (0.08 (red) and 1.26 m (blue)), the total heat flux (black lines), and the temperature difference between 3 and 7 m (green lines) are plotted versus time in hours relative to the local sunrise for four periods: (a) 7–8 September 2009, (b) 8–9 September 2009, (c) 9–10 September 2009, and (d) 10–11 September 2009.

requires the existence of an inertial subrange, as well as local isotropy. There is evidence that both assumptions are reasonably satisfied for wave breaking turbulence in the near-surface layer [*Gemmrich and Farmer*, 2004; *Gemmrich*, 2010] and as discussed in the Discussion below.

[11] The float follows the orbital motion of the larger waves, and hence the turbulence velocity fluctuations are given as

$$v'(z,t) = v(z,t) - \overline{v(t)}, \tag{3}$$

where $\overline{v(t)}$ is the mean velocity of the entire profile. (Although any constant velocity offset does not affect the structure function). Here we take the averaging period, denoted by $\langle\rangle$ above, as 0.4 s, i.e., eight consecutive samples. Thus, the dissipation field is estimated at a sampling rate of 2.5 Hz and with 6×10^{-3} m vertical resolution. The crests of riding waves, however, are outside the range of the turbulence profiles.

[12] Meteorological and oceanographic data, including wind speed, total heat flux, and significant wave heights, were obtained from an extensive set of instruments deployed on *FLIP* (the ongoing special section "Recent Advances in the Study of Optical Variability in the Near-Surface and Upper Ocean" in *Journal of Geophysical Research*; C. J. Zappa et al., An overview of sea state conditions and air-sea fluxes during RaDyO, submitted to *Journal of Geophysical Research*, 2011).

3. Results

[13] The main focus of this paper is on data collected during the period from 6 to 13 September 2009, when most of our sensors where operating simultaneously. All times used here are in UTC, and during this period the mean wind speeds varied between 5 and 7 m s^{-1}, but with a few periods where the wind speeds at height of 10 m, U_{10}, reached 9 to 10 m s^{-1}, notably during 8 September and from midday on 10 September to the beginning of 12 September (Figure 2a).

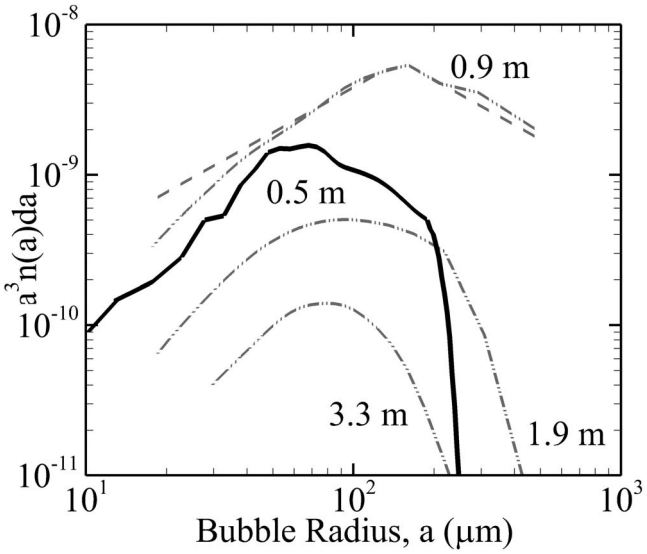

Figure 4. Volume-scaled bubble size distribution for the period from 7 to 12 September 2009 (solid black line). The dash-dotted lines represent averaged bubble size distributions from three depths obtained during an experiment in the Gulf of Mexico [*Vagle et al.*, 2010]. The dashed line is a parameterization of the 0.9 m size distribution as defined by equations (4)–(6) of *Vagle et al.* [2010].

During these periods the significant wave heights, H_s, ranged between 1.8 and 2.7 m. The total heat flux (Figure 2b) shows a strong diurnal signal throughout this period, with strong flux into the water around local noon and some heat loss during nighttime hours. The dashed lines in Figure 2b indicate times when the small temperature array was deployed from the R/V *Kilo Moana*.

[14] The near-surface temperature field from the thermistors on *FLIP* shows an overall decrease in temperature until just before midnight on 7 September, followed by a significant increase in surface water temperature from approximately 26.4°C to approximately 27.2°C by 11 September (Figure 2c). Between 7 September and halfway through 8 September there are extended periods with significant near-surface stratification, as indicated by the differences in temperatures between 3 and 15 m (Figure 2c). From 9 September and onward, there is a strong diurnal signal in the temperature records with well mixed water down to at least 15 m during most of the time, except for a number of hours around local noon when significant stratification is taking place. This stratification will be discussed further later on.

[15] Figure 2d shows turbulence dissipation rates ε (m^2 s^{-3}) (equation (2)) averaged over 8 min in time and between 0.14 and 0.75 m in range for the upward and between 1.04 and 1.76 m for downward pointing 2 MHz Dopbeam sonars on the surface following float deployed from *FLIP*. Here as well there is a strong observable diurnal signal with an order of magnitude differences in dissipation rates. Furthermore, the downward pointing sensor indicates higher dissipation rates than those observed closer to the surface, except for a few short periods. The gaps in the data represent times when the instrumentation was shut down for servicing and data downloads.

[16] The corresponding depths of the bubble plumes as observed with one of the 100 kHz backscatter sonars mounted at a depth of 34 m on *FLIP*'s hull are shown in Figure 2e. There is good correlation between wind speed and bubble penetration depth and during the wind event on 8 September, the bubbles were observed reaching depths of more than 20 m.

3.1. The Effect of Large Downward Heat Flux on Turbulence Dissipation Rates

[17] It is clear from the results presented in Figure 2d that large positive heat flux has a significant effect on the turbulence kinetic energy near the ocean surface. Our results show an order of magnitude reduction in the turbulence dissipation rate ε during the period of the day with strong positive heat flux. Some of this reduced rate might be due to stratification effects by bubbles [*Gemmrich*, 2000], but this can only explain a small fraction of the overall reduction.

[18] In Figure 3 the logarithm of the normalized turbulence dissipation rates $\varepsilon/\varepsilon_0$ is plotted versus time in hours relative to the local sunrise, for two depths (0.08 (red) and 1.26 m (blue)). Dissipation rates are normalized by their average rates from -10 to -2 h ε_0 at the specific depth bin. Also plotted with the same x axis are the measured total heat flux (black), wind stress τ (W m^{-2}) and the temperature difference between 3 and 7 m (green), used as a proxy for local stratification in our study. The maximum solar radiation occurred approximately 6 h after sunrise, while except for 7–8 September (Figure 3a), the maximum stratification happened 3 h after that, or 9 h after sunrise. The breakdown of the stratification coincided with the afternoon decrease in solar radiation. In all cases the turbulence dissipation rates show significantly lower values starting approximately 3 h after sunrise with minimum values around 11 h after sunrise on 7–8, 8–9, 9–10, and 10–11 September over the depth range from 0.08 to 1.26 m. During 10–11 September there is

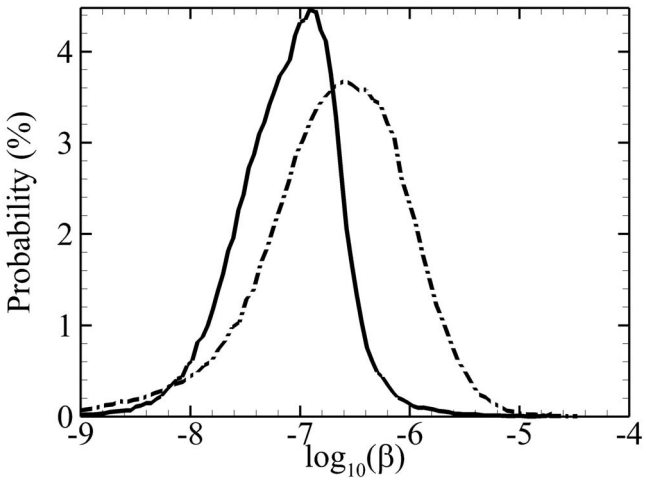

Figure 5. Solid line is the probability function of the logarithm of all air fraction values, β, for the period from 7 to 12 September. Using the parameterizations of the 0.9 m size distribution shown as a dashed line in Figure 4 and fitting the observations at a radius of 40 μm and shifted accordingly resulted in the probability distribution shown as the dash-dotted line.

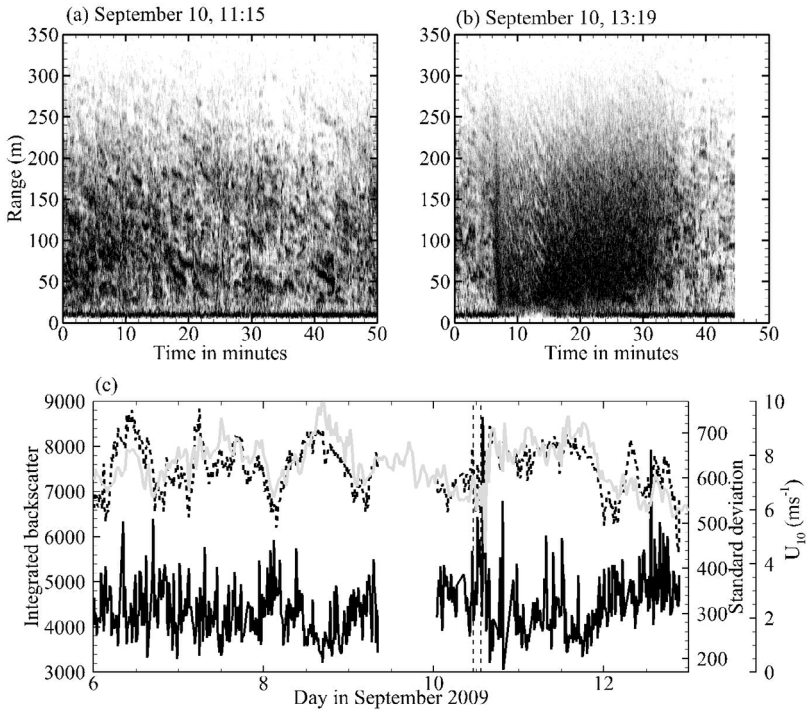

Figure 6. (a) Uncalibrated backscatter intensity data from a 100 kHz side scan sonar mounted at a depth of 34 m on *FLIP*'s hull for a 50 min period starting at 1115 UTC on 10 September 2009. (b) The same as in Figure 6a except that the data starts at 1319 UTC on 10 September 2009. (c) Range integrated uncalibrated backscatter intensities averaged over 15 min, for the duration of the experiment (dash-dotted line), the corresponding standard deviation (black solid line) and U_{10} (gray solid line). The two vertical dashed lines indicate the periods of the data shown in Figures 6a and 6b.

also enhanced near-surface turbulence just prior to sunrise and in the early afternoon due to limited periods of increased wind stress (Figure 3d). Generally, the turbulence dissipation rates at 0.08 and at 1.26 m behave very similar during the hours before sunrise. However, during the period with reduced turbulence our results show that the level is generally more suppressed near the surface, as can be seen in Figure 3, between 8 and 13 h after local sunrise.

3.2. Near-Surface In Situ Bubble Size Distributions

[19] Following the procedure outlined by *Farmer et al.* [1998] the 2–3 s acoustical spectra obtained from the resonator on the surface following float deployed from *FLIP* were inverted to get bubble size distributions. Even though the resonator used here was operating at frequencies between approximately 10 and 900 kHz, corresponding to bubble radii between approximately 5 and 300 μm, we are focusing on bubble radii between 10 and 300 μm in this study. In another study presented in this special section [*Czerski et al.*, 2011b] we are using the smaller bubbles to compare with independent optical measurements.

[20] Figure 4 (solid black line) shows an averaged bubble size distribution scaled by the radius cubed to better present the volume contribution by these bubbles to the overall air fraction for the period from 7 to 12 September 2009. For comparison we have also included averaged size distributions from three depths obtained during an experiment in the Gulf of Mexico at similar wind speeds but smaller heat fluxes [*Vagle et al.*, 2010]. There are significant differences between these observations. For bubbles with radii between 20 and 50 μm the distributions are nearly identical. However, for larger bubbles the present Hawaii size distribution falls off rapidly with increasing radii. For bubbles with radii between 90 and 100 μm the numbers per cubic meter of water at a depth of 0.5 m off Hawaii are similar to those in the Gulf of Mexico at 1.9 m while bubbles with radii greater than 250 μm were absent off Hawaii.

[21] To investigate this difference further we calculated the air fraction β from the bubble size distributions using

$$\beta = \frac{4\pi}{3} \int_{a=10}^{300} a^3 n(a) da, \tag{4}$$

where a is the bubble radius and $n(a)da$ is the number of bubbles per cubic meter of a given size a within a 1 μm radius increment. The integration was performed to cover bubbles with radii between 10 and 300 μm. In Figure 5 a probability function of the logarithm of all β for the period from 7 to 12 September is shown as a black solid line. The curve shows that the noise threshold of this sensor is 10^{-9}; in good agreement with previous instruments of this kind [*Vagle and Farmer*, 1998]. It is also apparent from these results that most of the size distributions observed have air fractions between 10^{-8} and 10^{-6}, and only a few times did the air fraction exceed 10^{-6}, which is quite low. For a comparison we made use of the fact that the shape of the measured averaged bubble size distribution is similar to

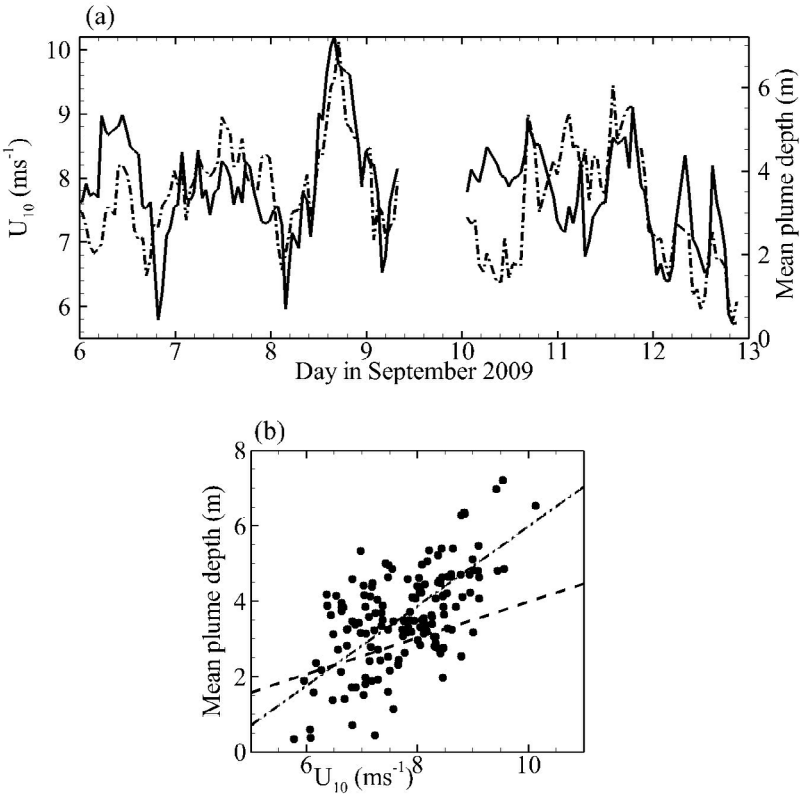

Figure 7. (a) Wind speed at 10 m height, U_{10}, (dash-dotted line) and mean bubble plume penetration depth δ_m (solid line) averaged over 2 1/4 h as obtained from a 100 kHz side scan sonar on *FLIP*'s hull. (b) The δ_m plotted against U_{10} for the data shown in Figure 7a. The dash-dotted line represents the linear least squares fit $\delta_m = -4.58 + 1.056U_{10}$ with $R^2 = 0.4$, and the dashed line is a fit from *Vagle et al.* [2010] ($\delta_m = -0.83 + 0.481U_{10}$ obtained from a different data set).

earlier distributions (dashed line in Figure 4) for bubbles with radii less than 50 μm. The parameterizations of the 0.9 m size distribution obtained from equations (4)–(6) of *Vagle et al.* [2010], were therefore scaled to fit the observed size distributions for radii <50 μm. The resulting probability distribution is shown as the dash-dotted line in Figure 5. The air fractions in this case cover the range from 10^{-8} to 10^{-5}, which is close to the saturation level of the resonator and more in line with earlier observations at similar wind speeds [*Vagle and Farmer*, 1998]. The absence of bubbles with radii greater than 250 μm in this study, are clearly lowering the overall observed air fractions, compared to the earlier Gulf of Mexico study. The exercise above also shows that the concentrations of bubbles with radii less than 250 μm are similar in the two studies, at the same wind speeds.

3.3. Spatial and Temporal Bubble Field Variability

[22] The bubble field around *FLIP*, to a range of approximately 300 m, was characterized using the four orthogonal 100 kHz backscatter sonars mounted on the hull. Figure 6a shows a typical 50 min backscatter image, plotted versus horizontal range along the surface, from one of these sonars. Darker areas indicate stronger targets or bubble plumes. Also observed are tilted bands associated with coherent Langmuir Cell activity generating windrows. The temporal variability in this backscatter field can be characterized by range integrating the noncalibrated backscatter amplitudes from 0 to 300 m. Figure 6c shows the integrated backscatter amplitudes (dashed line) averaged over 15 min and the corresponding standard deviation (solid line) for the period of interest. Also shown is the wind speed, U_{10} (solid gray line). As expected there is significant correlation between overall backscatter and wind speed ($R^2 = 0.7$). Also, as the wind speed and backscatter decreases, the standard deviation increases because of a decrease in the number of breaking waves and their turbulent energy, resulting in increased temporal variability in the injection of bubbles in our measurement area [*Gemmrich and Farmer*, 1999]. An exception to this scenario was a 4–5 h period on 10 September when 20 min periods with strong backscatter was followed by 10–20 min of the more expected backscatter levels. An example period is presented in Figure 6b. The corresponding patchiness, as indicated by the standard deviation shown in Figure 6c is clearly very high. No corresponding patchiness was observed in the meteorological data. However, anomalously deep bubble plumes were observed during this period, as discussed next.

[23] Using the same sonar system the penetration depth of the bubble field can also be estimated from the backscatter amplitude data between the transducer and the ocean surface, as shown in Figure 2e. The bubble plume depths were obtained from an amplitude threshold at which the backscatter strength rapidly approaches the noise level of the

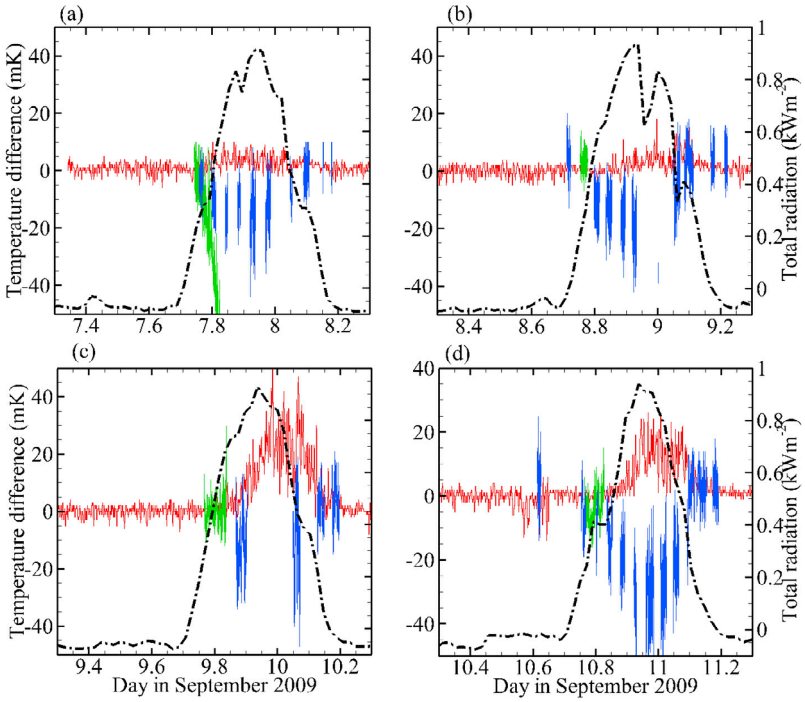

Figure 8. Time series of temperature differences relative to the thermistor at 3 m depth on *FLIP* for 4 days: (a) 7–8 September, (b) 8–9 September, (c) 9–10 September, and (d) 10–11 September. The red lines show the differences between the 3 and 7 m sensors. The green lines show the differences between the 3 m sensor on *FLIP* and the 0.1 m sensors on the small float deployed from *Kilo Moana*, approximately 2 km away. The blue lines show the temperature differences between the 3 m *FLIP* temperature sensor and the 0.4 m sensor on the surface following float deployed from *FLIP*. Also shown are the total heat flux measurements from *FLIP* (dash-dotted lines).

sonars and averaged over 2 1/4 h to allow for comparisons with similar data from a mooring in the North East Pacific [*Vagle et al.*, 2010]. *Vagle et al.* [2010] found that the estimated plume depths were quite insensitive to the choice of threshold value.

[24] Figure 7a shows the mean bubble penetration depth (solid line) plotted with the local wind speed (dash-dotted line). As expected, there is a reasonable correlation between mean bubble plume depth δ_m and wind speed except for three periods during the early hours of 6, 10, and 11 September. During the first two periods, between approximately 0000 and 1600 on 6 and 10 September, the observed averaged wind speeds were relatively low while the observed bubble field penetration depths exceeded 4 m; more than twice of expected depth. These anomalous events correspond to periods when significant patchiness was observed in the horizontal bubble field (Figure 6b). We hypothesize that short-term gustiness in the wind, during these periods generated the required vertical turbulent field and coherent flows to generate enough and pull the bubbles into the water column to the depths observed. The third event, during the early hours of 11 September, when the bubbles were not transported to the depth expected based on the observed wind speed, will be discussed in section 4.

[25] Figure 7b shows the relationship between wind speed, adjusted to 10 m height, U_{10} in ms^{-1}, and the average bubble plume depth. The dash-dotted line represents the least squares linear fit $\delta_m = -4.58 + 1.056U_{10}$, $R^2 = 0.4$. The dashed line is the relationship $\delta_m = -0.83 + 0.481U_{10}$, obtained previously from a different data set [*Vagle et al.*, 2010]. These results suggest that bubbles may be penetrating deeper during the Hawaii study than at the site in the North East Pacific. However, the acoustical sonar frequencies were different, with the present study using 100 kHz relatively wide beam sonars as compared to the 200 kHz narrow beam sonar used during the *Vagle et al.* [2010] study. The resonant bubble radius at 100 kHz is near 30 μm, which is close to the dominant bubble radius observed during the present study (Figure 4). Also, the relatively low R^2 value observed in the present study reflects the significant scatter observed in Figure 7b as a result of the anomalous periods discussed above.

4. Discussion

[26] Our results show that the turbulence dissipation rates were heavily modulated, following the diurnal cycle of total heat flux (Figures 2 and 3). During periods with high downward heat flux, dissipation rates were suppressed by an order of magnitude. In general, the results also show that the observed dissipation rates between 1.04 and 1.76 m from the instantaneous surface were higher than the dissipation rates between 0.14 and 0.72 m. We associate this with suppressed near-surface turbulence due to large near-surface temperature gradients as a result of the strong diurnal heat flux cycle. Reduced dissipation rates due to stratification has been observed previously within bubble plumes, and turbulence suppression was found to be a function of the buoyancy

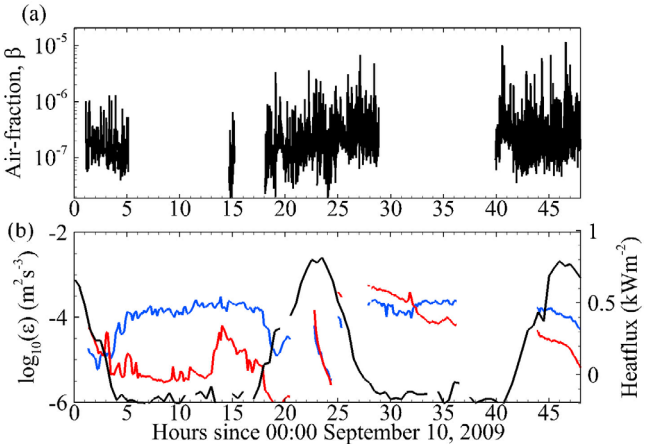

Figure 9. (a) Air fraction β versus time for a 45 h section starting at 0000 UTC on 10 September 2009. (b) Turbulence dissipation rate, ε, averaged between depths of 0.14 and 0.75 m (upward, red line) and between 1.04 and 1.76 m (downward, blue line) and the total heat flux (black line).

frequency N^2 [*Gemmrich and Farmer*, 2003]. Here we argue that dissipation decreases by a factor 10 due to strong near-surface thermal stratification and $N^2 = \alpha g\, dT/dz$, where α is the thermal expansion coefficient and g is the gravitational acceleration. Based on the results by *Gemmrich and Farmer* [2003] this observed reduction in dissipation corresponds to $N^2 \approx 3 \times 10^{-4}$ s^{-2}. Our observations of temperature gradients close to the surface are limited, but the required temperature gradient of 0.1 K m^{-1} is consistent with the 30 mK difference between 0.1 and 0.4 m depth indicated in the short record of Figure 8a. Furthermore, the longer temperature records at 0.4 and 3 m depth clearly show that near-surface stratification could persist despite the likely presence of shear-driven and wave-induced turbulence (Figure 8). Note, these estimates imply the Ozmidov-scale $L_O > 1$ m, i.e., stratification mainly affects the energy containing eddies, and therefore the assumption of isotropy used in equation (2) is still applicable.

[27] In the early hours of 11 September the wind increased while the depth of the bubble layer stayed steady, or actually dropped a little (Figure 7a). This period represented the time during this experiment when we observed the strongest stratification, as shown in Figure 8d where the temperature difference between 0.4 and 3 m exceeded 40 mK. We hypothesize that this strong stratification and the relatively short duration of the wind event, limited the vertical extent of the bubble mixing. Also during the same period the diurnal turbulence pattern changed and the near-surface turbulence was stronger than the turbulence below 1 m depth (Figure 9b). Included in Figure 9a is the observed time series of the air fraction, showing very little variability around this period. The period with enhanced near-surface turbulence and a relatively shallow bubble layer suggest that the energy from the relatively short wind event was used to increase the turbulence in a shallow near-surface layer only as a result of the strong stratification.

[28] It is worth noting that a relationship between temperature and the bubble distribution has been reported before. *Bortkovskii* [1987] observed a shift toward smaller bubbles with increasing temperature and a positive dependence of whitecap coverage upon sea surface temperature. In addition to the observed overall reduction in expected concentrations of bubbles with radii larger than approximately 50 μm during this experiment, we wanted to investigate whether it was possible to observe differences in the bubble size distributions between stable (positive heat flux) and unstable (negative heat flux) conditions at this location. In Figure 10 all available bubble size distributions from periods with positive heat flux during the 3 days: 7, 8, and 10 September, have been averaged for each period (Figure 2b) (blue lines) and shown with the corresponding averaged distributions from periods with negative heat flux during those days (red lines). The results suggest that there may be slightly higher number of bubbles with radii between 20 and 200 μm during stable conditions. However, the most significant difference seems to be for bubbles larger than 200 μm. Unfortunately, the instrumentation used during this experiment was not capable of observing bubbles with radii greater than approximately 300 μm. Nevertheless, there are clear indications that during the stable conditions, the number of larger bubbles is significantly

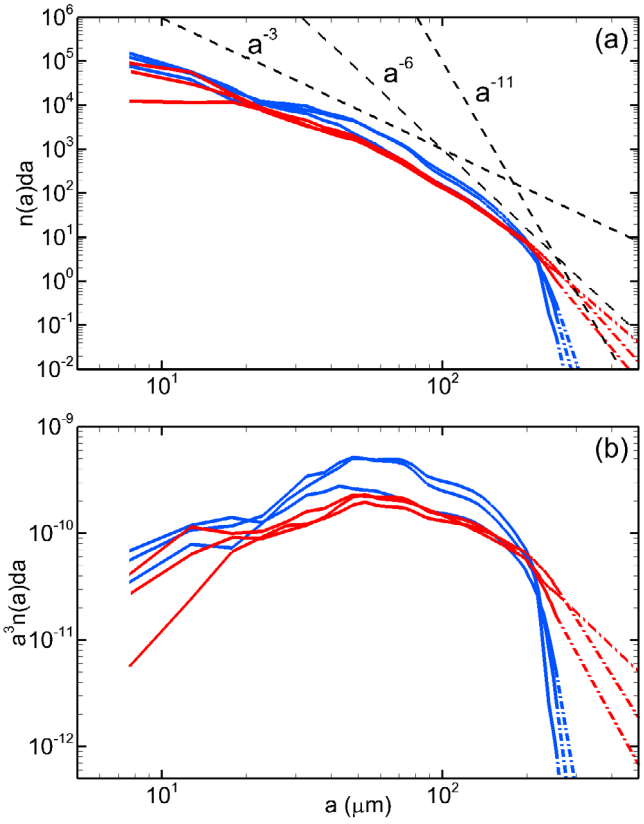

Figure 10. (a) Three daily averaged bubble size distributions from 7, 8, and 10 September for periods when the heat flux was positive (stable conditions) (blue lines) and the corresponding averages for periods with negative heat flux (unstable conditions) (red lines). The dash-dotted lines are logarithmic extrapolations to bubble radii exceeding the current measurement range. Also shown are three different slopes, as discussed in the text (dashed lines). (b) The same distribution scaled by the cubed of the bubble radius.

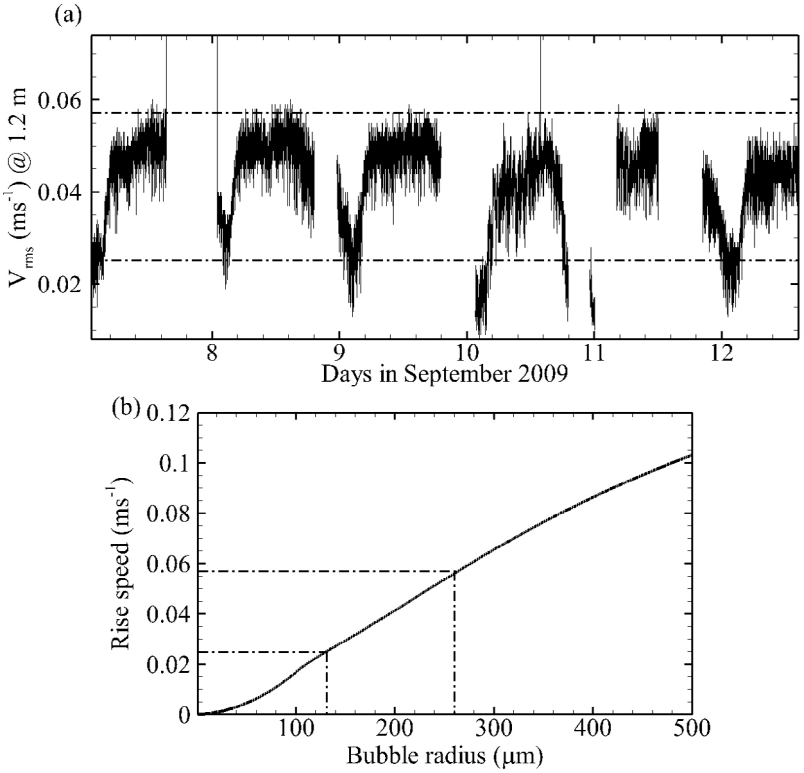

Figure 11. (a) RMS velocities calculated over 0.05 m and averaged over 30 s at a depth of 1.2 m. (b) Terminal rise speed of bubbles for a range of bubble radii between 1 and 500 μm. The dash-dotted lines in show that lower observed RMS fluid velocity value correspond to bubbles with a radius of 130 μm, while the unstable conditions RMS fluid velocity value correspond to bubbles with a radius of 260 μm.

reduced. For bubbles with radii between 8 and 100 μm the slope of the bubble size distribution is proportional to a^{-3} for both conditions. However, during unstable conditions the slope of the bubble size distribution is closer to a^{-6} for larger bubbles, while for stable conditions this decreases to approximately a^{-11}. The dash-dotted lines are logarithmic extrapolations to larger bubble radii.

[29] The relationship between the observed variability in upper ocean turbulence and the inferred bubble size distributions can be investigated by considering the range of flow velocities available to bring bubbles generated by breaking waves into the water column against their buoyancy. Figure 11a shows the RMS velocities calculated over 0.05 m and averaged over 30 s at a depth of 1.2 m. The velocities cover a range between 0.02 and 0.06 m s^{-1}. The terminal rise speed of bubbles can be obtained from the balance between drag and buoyancy forces. Here we use the equation presented by *Vagle et al.* [2005], which was based on *Keeling* [1993] and *Levich* [1962]. This rise speed has been plotted for bubble radii between 1 and 500 μm in Figure 11b. The dash-dotted lines in Figure 11b show that observed low RMS fluid velocity value (0.02 m s^{-1}) corresponding to bubbles with a radius of 130 μm and the RMS fluid velocity during unstable conditions (0.06 m s^{-1}), corresponding to bubbles with a radius of 260 μm. As the upper water column stabilizes and the turbulence decreases, the velocity field can no longer suspend bubbles with radii greater than 130 μm and the slope of the bubble size distribution decreases.

[30] A number of studies have suggested that bubble plumes play a significant role in scattering light in the upper ocean and are therefore important to remote sensing reflectance [e.g., *Stramski*, 1994; *Zhang et al.*, 1998; *Terrill et al.*, 1998]. *Stramski and Tegowski* [2001] showed that the remote sensing reflectance can increase more than twofold with the presence of bubbles. Light-scattering properties of bubbles suspended in water can be calculated with Mie theory. Following the development by *Stramski and Tegowski* [2001] one can calculate a volume-scattering cross section due to bubbles, $\sigma_{bub}(\lambda)$, at a given light wavelength, λ, and at 0.5 m, the depth of our bubble size distributions, as

$$\sigma_{bub}(\lambda) = \frac{\int_{a=10}^{300} \pi a^2 Q_b(a,\lambda) n(a) da}{\int_{a=10}^{300} n(a) da}, \quad (5)$$

where $Q_b(a, \lambda)$ is the dimensionless scattering efficiency factor [*Bohren and Huffman*, 1983] at λ for a bubble with radius a. The integration is performed over the available bubble radii between 10 and 300 μm. Figure 12a shows $\sigma_{bub}(\lambda)$ calculated for a 2 h period early on in the experiment, showing variability of 3 orders of magnitude in the

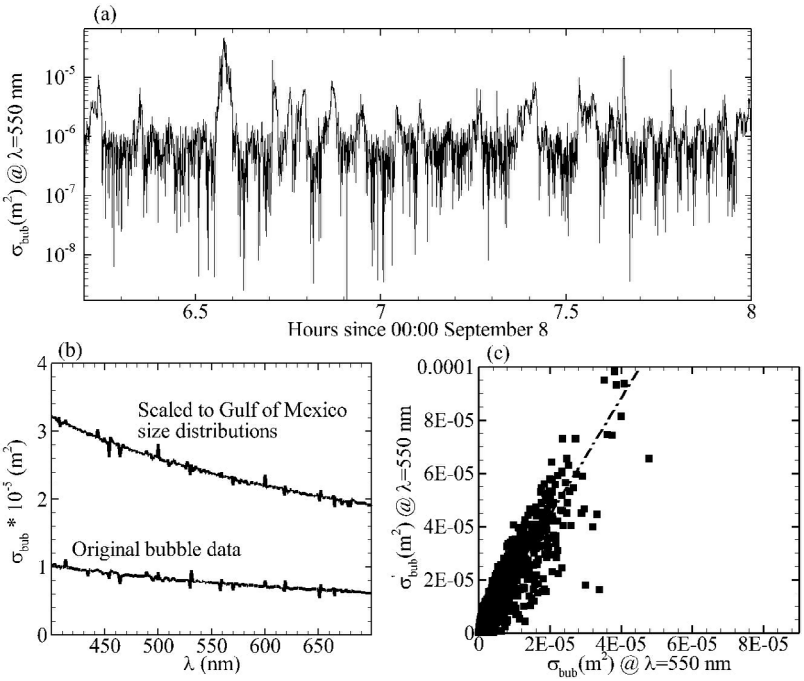

Figure 12. (a) Volume-scattering cross section due to bubbles, σ_{bub} calculated at a light wavelength λ of 550 nm from the bubble size distributions obtained at a depth of 0.5 m for a 2h period on 8 September 2009. (b) The σ_{bub} calculated as a function of λ for the averaged bubble size distribution shown in Figure 4 (lower black line) and scaled using the Gulf of Mexico size distribution (upper black line). (c) The σ_{bub} plotted against the volume-scattering cross section due to bubbles calculated using the scaled size distributions, $\sigma_{bub}^{'}$ at λ = 550 nm. The dash-dotted line shows a fitted ratio of 2 with R^2 = 0.85.

scattering cross sections at λ = 550 nm. Using both the averaged observed bubble size distribution shown in Figure 4 and a bubble size distribution obtained using the 0.9 m distribution from the Gulf of Mexico data set, $\sigma_{bub}(\lambda)$ and $\sigma_{bub}^{'}(\lambda)$ were calculated as functions of light wavelength using equation (5) (Figure 12b). It is clear that due to the omission of the larger bubbles in the present study, the scattering cross section is as much as a factor of 3 lower, at the smallest λ, than in the earlier study. Again choosing a light wavelength of 550 nm, the ratio of the calculated $\sigma_{bub}(\lambda)$ and the predicted $\sigma_{bub}^{'}(\lambda)$ show a ratio of 2 with R^2 = 0.85 (Figure 12c).

5. Conclusions

[31] A unique data set of simultaneous measurements of upper ocean turbulence, bubble size distributions, heat flux, and temperature stratification collected during the Hawaii RaDyO experiment has shown that strong positive heat flux modulate both the turbulence dissipation levels and the bubble size distributions on diurnal timescales. Although the observations of near-surface temperature stratification are limited, the available data strongly suggest that such stratification did occur and that the observed temperature gradients were sufficient to suppress turbulence dissipation by the order of magnitude observed.

[32] Also, the overall concentration of bubbles with radii greater than 100 μm was found to be lower during this study than another study in the Gulf of Mexico, at similar wind speeds. Suppressed near-surface turbulence reduces the downward advection of bubbles against their size-dependent buoyant rise speed, resulting in fewer larger bubbles with depth. However, it is also possible that strong positive heat flux reduces the intensity of individual breakers and their capability of generating larger bubbles. For example, *Manasseh et al.* [2006] observed a relationship between the strength of breaking waves and the size of the bubbles being produced. The relationship between strong heat flux and breaker intensity is presently being investigated in another study. The observed variability in the composition of the bubble size distribution has significant potential impacts on the overall air fraction and on upper ocean light reflectance.

[33] We argue that strong stratification in these waters play a significant role in controlling both the turbulence and subsequently the bubble field. However, surfactants may also play an important role, especially for the overall reduced larger radii bubbles. Measurements of surfactants during the field experiment suggest that there were significant amounts of surface active substances present in the area [*Wurl et al.*, 2011]. Further studies are necessary to determine the role of these compounds on the upper ocean physical processes.

[34] **Acknowledgments.** We appreciate all the work done by Nick Hall-Patch at the Institute of Ocean Sciences while constructing the acoustical resonator used in this study and while operating the instrumentation onboard R/P *FLIP* during the field experiment. We acknowledge the support and guidance from officers and crews onboard R/P *FLIP* and R/V *Kilo Moana*. The meteorological data were provided by Luc Lenain. We also are grateful for a number of useful comments from three anonymous reviewers. This work was carried out as part of the Office of Naval Research funded Radiance in a Dynamic Ocean (RaDyO) program through contracts

N000140610072, N000140610379, and N000140710015. The support from Fisheries and Oceans Canada is also greatly appreciated.

References

Bohren, C. F., and D. R. Huffman (1983), *Absorption and Scattering of Light by Small Particles*, John Wiley, New York.

Bortkovskii, R. S. (1987), *Air-Sea Exchange of Heat and Moisture During Storms*, 124 pp., D. Reidel, Norwell, Mass.

Commander, K. C., and R. J. McDonald (1991), Finite-element solution of the inverse problem in bubble swarm acoustics, *J. Acoust. Soc. Am.*, *89*, 592–597, doi:10.1121/1.400671.

Czerski, H., S. Vagle, D. M. Farmer, and N. Hall-Patch (2011a), Improvements to the methods used to measure bubble attenuation using an underwater acoustical resonator, *J. Acoust. Soc. Am.*, *130*, 3421–3430.

Czerski, H., M. Twardowski, Z. Zhang, and S. Vagle (2011b), Resolving size distributions of bubbles with radii less than 30 μm with optical and acoustical methods, *J. Geophys. Res.*, *116*, C00H11, doi:10.1029/2011JC007177.

Deane, G. B., and M. D. Stokes (2002), Scale dependence of bubble creation mechanisms in breaking waves, *Nature*, *418*, 839–844, doi:10.1038/nature00967.

Farmer, D. M., S. Vagle, and A. D. Booth (1998), A free-flooding acoustical resonator for measurement of bubble size distributions, *J. Atmos. Oceanic Technol.*, *15*, 1132–1146, doi:10.1175/1520-0426(1998)015<1132:AFFARF>2.0.CO;2.

Farmer, D. M., S. Vagle, and A. D. Booth (2005), Reverberation effects in acoustical resonators used for bubble measurements, *J. Acoust. Soc. Am.*, *118*, 2954–2960, doi:10.1121/1.2047148.

Garrett, C., M. Li, and D. M. Farmer (2000), The connection between bubble size spectra and the energy dissipation rates in the upper ocean, *J. Phys. Oceanogr.*, *30*, 2163–2171, doi:10.1175/1520-0485(2000)030<2163:TCBBSS>2.0.CO;2.

Gemmrich, J. (2000), Temperature anomalies beneath breaking waves and the decay of wave-induced turbulence, *J. Geophys. Res.*, *105*, 8727–8736, doi:10.1029/1999JC900322.

Gemmrich, J. (2010), Strong turbulence in the wave crest region, *J. Phys. Oceanogr.*, *40*, 583–595, doi:10.1175/2009JPO4179.1.

Gemmrich, J. R., and D. M. Farmer (1999), Observations of the scale and occurrence of breaking surface waves, *J. Phys. Oceanogr.*, *29*, 2595–2606, doi:10.1175/1520-0485(1999)029<2595:OOTSAO>2.0.CO;2.

Gemmrich, J. R., and D. M. Farmer (2003), Observations of near-surface turbulence within bubble plumes, *Eos Trans. AGU*, *84*(52), Ocean Sci. Meet. Suppl., Abstract OS411-09.

Gemmrich, J. R., and D. M. Farmer (2004), Near-surface turbulence in the presence of breaking waves, *J. Phys. Oceanogr.*, *34*, 1067–1086, doi:10.1175/1520-0485(2004)034<1067:NTITPO>2.0.CO;2.

Keeling, R. F. (1993), On the role of large bubbles in air-sea gas exchange and supersaturation in the ocean, *J. Mar. Res.*, *51*, 237–271, doi:10.1357/0022240933223800.

Levich, V. G. (1962), *Physico-Chemical Hydrodynamics*, Prentice Hall, New York.

Manasseh, R., A. V. Babanin, C. Forbes, K. Rickards, I. Bobevski, and A. Ooi (2006), Passive acoustic determination of wave-breaking events and their severity across the spectrum, *J. Atmos. Oceanic Technol.*, *23*, 599–618, doi:10.1175/JTECH1853.1.

Stramski, D. (1994), Gas microbubbles: An assessment of their significance to light scattering in quiescent seas, in *Ocean Optics XII*, vol. 2258, edited by J. S. Jaffe, pp. 704–710, Int. Soc. for Opt. Eng., Bellingham, Wash., doi:10.1117/12.190117.

Stramski, D., and J. Tegowski (2001), Effect of intermittent entrainment of air bubbles by breaking wind waves on ocean reflectance and underwater light field, *J. Geophys. Res.*, *106*, 31,345–31,360, doi:10.1029/2000JC000461.

Terrill, E. J., W. K. Melville, and D. Stramski (1998), Bubble entrainment by breaking waves and their effects on the inherent optical properties of the upper ocean, paper presented at Ocean Optics XIV, Off. of Nav. Res., Kailua-Kona, Hawaii.

Thorpe, S. A. (1992), Bubble clouds and the dynamics of the upper ocean, *Q. J. R. Meteorol. Soc.*, *118*, 1–22, doi:10.1002/qj.49711850302.

Vagle, S., and D. M. Farmer (1998), A comparison of four methods for bubble size and void fraction measurements, *IEEE J. Oceanic Eng.*, *23*, 211–222, doi:10.1109/48.701193.

Vagle, S., P. Chandler, and D. M. Farmer (2005), On the dense bubble clouds and near bottom turbulence in the surf zone, *J. Geophys. Res.*, *110*, C09018, doi:10.1029/2004JC002603.

Vagle, S., C. McNeil, and N. Steiner (2010), Upper ocean bubble measurements from the NE Pacific and estimates of their role in air-sea gas transfer of the weakly soluble gases nitrogen and oxygen, *J. Geophys. Res.*, *115*, C12054, doi:10.1029/2009JC005990.

Wurl, O., L. Miller, and S. Vagle (2011), Production and fate of transparent exopolymer particles in the ocean, *J. Geophys. Res.*, *116*, C00H13, doi:10.1029/2011JC007342.

Zhang, X., M. Lewis, and B. Johnson (1998), Influence of bubbles on scattering of light in the ocean, *Appl. Opt.*, *37*, 6525–6536, doi:10.1364/AO.37.006525.

H. Czerski, Institute of Sound and Vibration Research, University of Southampton, Highfield, Southampton SO17 1BJ, UK.

J. Gemmrich, Department of Physics and Astronomy, University of Victoria, PO Box 3055, Victoria, BC V8W 3P6, Canada.

S. Vagle, Institute of Ocean Sciences, Fisheries and Oceans Canada, 9860 W. Saanich Rd., Sidney, BC V8L 4B2, Canada. (svein.vagle@dfo-mpo.gc.ca)